White dwarfs as a probe of exceptionally light QCD axions

Reuven Balkin,[1,*] Javi Serra[ORCID],[2,3,†] Konstantin Springmann[ORCID],[2,‡] Stefan Stelzl[ORCID],[2,4,§] and Andreas Weiler[ORCID][2,∥]

[1]*Physics Department, Technion—Israel Institute of Technology, Haifa 3200003, Israel*
[2]*Physik Department, Technische Universität München, 85748 Garching, Germany*
[3]*Instituto de Física Teórica UAM/CSIC, Madrid 28049, Spain*
[4]*Institute of Physics, Theoretical Particle Physics Laboratory, École Polytechnique Fédérale de Lausanne, CH-1015 Lausanne, Switzerland*

We study the effects of exceptionally light QCD axions on the stellar configuration of white dwarfs. At finite baryon density, the nonderivative coupling of the axion to nucleons displaces the axion from its in-vacuum minimum, which implies a reduction of the nucleon mass. This dramatically alters the composition of stellar remnants. In particular, the modifications of the mass-radius relationship of white dwarfs allow us to probe large regions of unexplored parameter space without requiring that axions are dark matter.

I. INTRODUCTION

Recent years have seen a resurgence of interest in the physics of the QCD axion, driven by a thriving experimental program in sync with a burst of novel theoretical ideas. One instance is the possibility of relaxing the standard relation between the axion potential and its defining couplings to gluons. Arguably the most exciting outcome of these models is the new set of signals they give rise to beyond the canonical QCD-axion phenomena. Here we present a novel implication associated with exceptionally light QCD axions: white dwarfs (WDs) of a certain size should not exist. This leads to novel bounds on the QCD axion parameter space, Fig. 1.

We consider models of the QCD axion, a pseudoscalar field ϕ with a coupling to gluons

$$\mathcal{L} = \frac{g_s^2}{32\pi^2}\frac{\phi}{f}G_{\mu\nu}\tilde{G}^{\mu\nu}, \qquad (1)$$

where g_s is the strong coupling, f is the axion decay constant, and $G_{\mu\nu}$ is the gluon field strength. Below the QCD scale the axion obtains the potential [1]

$$V \simeq -\epsilon m_\pi^2 f_\pi^2\left[\cos\left(\frac{\phi}{f}\right) - 1\right], \qquad (2)$$

where $m_\pi \simeq 135$ MeV is the pion mass and $f_\pi \simeq 93$ MeV is the pion decay constant. A parameter $\epsilon \leq 1$ is introduced to tune the axion lighter than naively expected [2]. For a symmetry-based realization, see, e.g., [3–6], where note that around the origin and at finite density, these models are well parametrized by Eq. (2). While in the main text we focus on the simple potential Eq. (2) , a full analysis and discussion of the modifications due to the form of the $Z_\mathcal{N}$ axion potential [4] is presented in Appendix C. In vacuum, the axion is stabilized at the origin, thereby solving the strong CP problem.

The coupling to gluons, Eq. (1), also induces an isospin-symmetric coupling to nucleons

$$\mathcal{L} \simeq -\sigma_N \bar{N}N\left[\cos\left(\frac{\phi}{f}\right) - 1\right], \qquad (3)$$

where $\sigma_N \simeq 50$ MeV is the pion-nucleon σ term. Together with the observed mass, $m_N \simeq 939$ MeV, this coupling can be interpreted as an effective ϕ-dependent nucleon mass, $m_N^*(\phi) \leq m_N$.

A finite nucleon number density, $\rho_N \equiv \langle\bar{N}\gamma^0 N\rangle$, implies a nonzero expectation value of $\langle\bar{N}N\rangle$. In the nonrelativistic limit, these two quantities are approximately equal, $\rho_N \simeq \langle\bar{N}N\rangle$.

Interestingly, a finite ρ_N can destabilize the axion from its in-vacuum minimum as soon as $\sigma_N\langle\bar{N}N\rangle > \epsilon m_\pi^2 f_\pi^2$, with new minima appearing at $\pm\pi f$ [2,7]. Furthermore, once the axion sits in its new minimum, the neutron mass is reduced by

---
[*]reuven.b@campus.technion.ac.il
[†]javi.serra@ift.csic.es
[‡]konstantin.springmann@tum.de
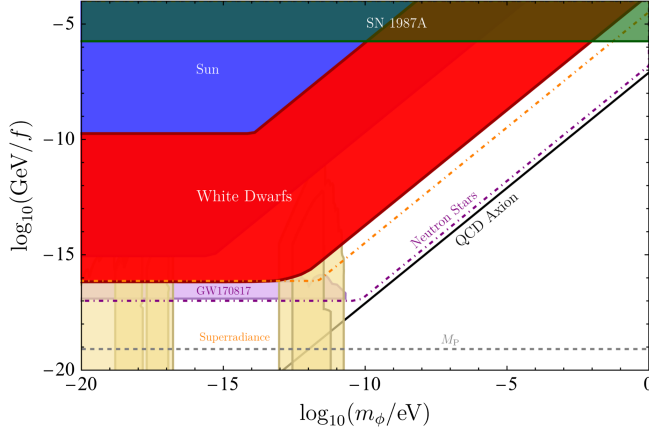[§]stefan.stelzl@epfl.ch
[∥]andreas.weiler@tum.de

FIG. 1. Constraints and future projections on the axion parameter space for the ϵ model. Exclusions from modifications of the white dwarf M–R relation are shown in red. Note that the WD bound overlaps with bounds from the Sun in large parts of the region (slightly darker red). The observation of WDs close to the Chandrasekhar limit can further probe the parameter space until the orange dashed line. The solid black line shows the QCD axion with $m_\phi f = m_\pi f_\pi$. For reference, we plot $f = M_P$ in gray. Further bounds originate from the sourcing in the Sun [2] (blue) and the gravitational wave signal of the neutron star binary GW170817 [11] (violet), which we both adapted at large f according to numerically inspired $\mathcal{O}(1)$ factors, the supernova 1987A [12] (green), and black hole superradiance [13] (yellow). We would furthermore like to note that the pulsar bound of [2] goes away once all finite gradient effects are properly taken into account (besides lying within a region that is strongly dependent on the neutron star EOS) [9]. Finally, we show which parameters lead to a new ground state accessible in neutron stars (dot-dashed purple); for more details see [9].

$$\delta m_N \simeq 32 \text{ MeV} \left(\frac{\sigma_N}{50 \text{ MeV}} \right). \qquad (4)$$

Reducing the constituent mass acts as additional binding energy in compact objects.

The sourcing of ϕ happens in nonrelativistic systems of size R when

$$R \gtrsim \lambda_\phi \simeq 10^4 \text{ km} \left(\frac{f}{10^{16} \text{ GeV}} \right) \left(\frac{10^{-4} \text{ MeV}^3}{\rho_N} \right)^{1/2}, \quad (5)$$

where $\lambda_\phi \sim m_\phi^{-1}(\rho_N)$ is the typical length scale of the axion at finite density [2,8,9], see also Eq. (13). Typical WD densities fall in the range $\rho_{\text{WD}} \simeq (10^{-4}\text{–}1 \text{ MeV})^3$. This implies that, for systems with a small characteristic length scale, such as single nuclei, the axion remains stabilized at $\phi = 0$ and therefore does not significantly affect forces between nucleons.

However, for large and dense systems such as stellar remnants, the sourcing of ϕ implies dramatic changes in their composition and hence their mass-radius (M–R) relation. A particularly clean and well-studied example
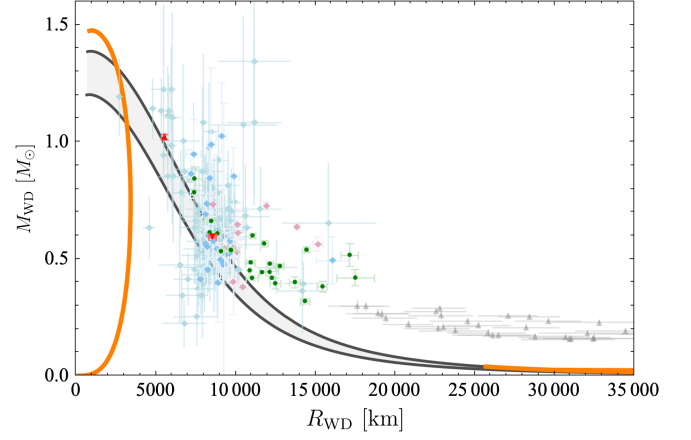

FIG. 2. White dwarf M–R relation with light QCD axions. Free Fermi gas of nuclei and electrons without an axion (black). The upper and lower bands correspond to the constitutions of light and more heavy nuclei, i.e., ^{4}He which corresponds to $Y_e = 2$ and ^{56}Fe corresponding to $Y_e = 2.15$, respectively, while the gray shaded area corresponds to intermediate values. In orange we show the two branches with an axion for $\epsilon = 10^{-11}$ in the limit $R_{\text{WD}} \gg \lambda_\phi$ for $Y_e = 2$. The metastable branch follows the free Fermi gas line at large radii, while the new ground state phase has much smaller radii. Data points are taken from [14] (turquoise), [15] (blue), [16] (pink), [17,18] (red), [19] (green), and [20] (gray). One can clearly see the gap in the predicted M–R relation that is incompatible with data.

of stellar remnants are WDs. The modifications of their M–R relation allow us to probe large regions in the light axion parameter space. For an exploratory study of axions and other particles influencing the stellar structure of neutron stars in the same manner, see [9,10].

II. WHITE DWARF MASS-RADIUS RELATION

WDs balance the force of gravity with the degeneracy pressure of electrons, while almost their entire mass comes from light but nonrelativistic nuclei. Because of charge neutrality, the number density of electrons is related to the energy density of nucleons, $\varepsilon_\psi \simeq Y_e m_N \rho_e$, where $Y_e = A/Z$ is the ratio of nucleons per electron. Since WDs are composed of light nuclei, ranging from helium ^{4}He to magnesium ^{24}Mg, the ratio of nucleons per electron is well approximated by $Y_e \simeq 2$, see also Fig. 2.

A. Noninteracting gas of electrons and nuclei

The equation of state (EOS) for a degenerate WD can be described by a Fermi gas of noninteracting electrons together with a gas of nuclei. For simplicity, we take positively charged nonrelativistic nuclei, which we denote by ψ, with twice the nucleon mass $m_\psi = 2m_N$. The pressure is dominated by the electron contribution, $p = p_e + p_\psi \simeq p_e$, while the nuclei constitute, to a good approximation, the entire energy density, $\varepsilon = \varepsilon_e + \varepsilon_\psi \simeq \varepsilon_\psi$.

Because of charge neutrality, $\rho_\psi = \rho_e \equiv \rho$, we relate the electron Fermi momentum to the energy density as $k_F = (3\pi^2 \varepsilon_\psi / Y_e m_N)^{1/3}$, and derive the EOS

$$p(\varepsilon) = \frac{2}{3} \int_0^{k_F(\varepsilon)} \frac{d^3 k}{(2\pi)^3} \frac{k^2}{\sqrt{k^2 + m_e^2}}. \tag{6}$$

We work in the limit $T \to 0$, which is justified since $T/\mu_e \ll 1$ for typical WDs, where μ_e is the electron chemical potential. Temperature shifts the M–R relation up to higher masses, an effect most relevant for the largest and most dilute WDs, see Refs. [19,21–26] as well as Ref. [27] for a review.

The EOS completes the set of equations that describe the balance between the electron degeneracy pressure and gravity, the Tolman-Oppenheimer-Volkoff (TOV) equations [28,29],

$$p' = -\frac{GM\varepsilon}{r^2} \left[1 + \frac{p}{\varepsilon} \right] \left[1 - \frac{2GM}{r} \right]^{-1} \left[1 + \frac{4\pi r^3 p}{M} \right], \tag{7a}$$

$$M' = 4\pi r^2 \varepsilon, \tag{7b}$$

where $G = M_{\rm P}^{-2}$ is Newton's constant, $M(r)$ is the enclosed mass, and all derivatives are taken with respect to the radial coordinate. Solutions with varying central pressures lead to a M–R relationship that agrees well with current data, as shown in Fig. 2.

B. The axion WD system: A new ground state

In the presence of the axion, the full system is described by a free Fermi gas of electrons, an ideal gas of nuclei with a ϕ-dependent mass [30], $m_\psi^*(\phi) = 2m_N^*(\phi)$, the gravitational field $g_{\mu\nu}$, and the axion ϕ. The gravitational field is sourced by an energy-momentum tensor

$$T_{\mu\nu} = T_{\mu\nu}^{\psi\phi} + T_{\mu\nu}^{\rm grad}. \tag{8}$$

The first term takes the form of an ideal fluid, $T_{\mu\nu}^{\psi\phi} = {\rm Diag}(\varepsilon, -p, -p, -p)$, with

$$p(\phi, \rho) = \frac{2}{3} \int_0^{k_F(\rho)} \frac{d^3 k}{(2\pi)^3} \frac{k^2}{\sqrt{k^2 + m_e^2}} - V(\phi), \tag{9}$$

$$\varepsilon(\phi, \rho) = m_\psi^*(\phi) \rho + \varepsilon_e(\rho) + V(\phi), \tag{10}$$

where we neglected the subleading contributions to the pressure $p_\psi(\phi, \rho) \ll p_e(\rho)$. The second term in Eq. (8) contains the contribution of the axion gradient

$$(T^{\rm grad})^\mu{}_\nu = \frac{(\phi')^2}{2} \left[1 - \frac{2GM}{r} \right] \left(\delta_\nu^\mu - 2\delta_r^\mu \delta_\nu^r \right). \tag{11}$$

Using Einstein's and the scalar equations of motion, we find the following set of coupled differential equations:

$$\phi'' \left[1 - \frac{2GM}{r} \right] + \frac{2}{r} \phi' \left[1 - \frac{GM}{r} - 2\pi G r^2 (\varepsilon - p) \right] = \frac{\partial V}{\partial \phi} + \rho \frac{\partial m_\psi^*(\phi)}{\partial \phi} \equiv U(\phi, \rho), \tag{12a}$$

$$p' = -\frac{GM\varepsilon}{r^2} \left[1 + \frac{p}{\varepsilon} \right] \left[1 - \frac{2GM}{r} \right]^{-1} \left[1 + \frac{4\pi r^3}{M} \left(p + \frac{(\phi')^2}{2} \left\{ 1 - \frac{2GM}{r} \right\} \right) \right] - \phi' U(\phi, \rho), \tag{12b}$$

$$M' = 4\pi r^2 \left[\varepsilon + \frac{1}{2} \left(1 - \frac{2GM}{r} \right) (\phi')^2 \right]. \tag{12c}$$

Equation (12a) is the static axion equation of motion coupled to gravity, while Eqs. (12b) and (12c) are the TOV equations in the presence of an axion. Note that we recover the ordinary TOV equations (7) in the limit $\phi = 0$. While it is possible to numerically solve Eq. (12) using the shooting method, there exists a limit in which these equations simplify dramatically.

The displacement of the axion at sufficiently high densities costs gradient energy and therefore it only occurs if balanced by the gain in potential energy. This leads to the typical scale on which the axion is displaced,

$$\lambda_\phi(\rho) \simeq \frac{\pi f}{\sqrt{2(\delta m_N \rho - \epsilon m_\pi^2 f_\pi^2)}}, \tag{13}$$

to be evaluated at typical WD densities.

For $R_{\rm WD} \gg \lambda_\phi$, the field essentially tracks the minimum of the effective in-density potential on stellar scales and is given by the solution to

$$U(\phi, \rho) = 0. \tag{14}$$

At the same time, the gradient terms in Eqs. (12b) and (12c) are confined to a small transition shell, where the field does not follow its minimum. However, this localized contribution is negligible as long as $\frac{\lambda_\phi}{R_{WD}} \frac{\delta m_N}{m_N} \ll 1$, which is trivially fulfilled in this case.

Therefore, for large systems, we can neglect the axion gradient $\phi' \simeq 0$. As a result, Eq. (12) decouples to give the regular TOV equations (7) in addition to Eq. (14). Note that the latter is the same condition as the minimization of the energy density $\varepsilon(\phi, \rho)$ with respect to ϕ. Solutions $\phi(\rho)$ describe a thermodynamically stable EOS used to solve the regular TOV equations.

Interestingly, if the axion is destabilized in a WD, the energy per particle of the light nuclei $\varepsilon(\rho)/\rho$ is not minimized when the nuclei are infinitely separated ($\rho \to 0$), but rather at some finite density ρ^*, which can be found numerically. This implies the existence of an energetically favored state of matter at ρ^*, where the axion is at $\langle\phi\rangle = \pm\pi f$. This new ground state is, in fact, reminiscent to strange quark matter [31]. Note that the density of the new ground state is slightly larger than the density at which the destabilization occurs, $\rho^* > \rho_c \equiv \epsilon m_\pi^2 f_\pi^2 / 2\sigma_N$.

For low densities $\rho < \rho_c$, matter is in a metastable state where the classical sourcing of the axion is not preferable. Once $\langle\phi\rangle = \pm\pi f$, there is a range $\rho_c < \rho < \rho^*$, where the energy per particle decreases $\partial_\rho(\varepsilon(\rho)/\rho) < 0$, implying a negative pressure. At densities slightly above ρ_c, the total pressure turns negative due to the onset of the axion potential $p = p_e - V < 0$. As ρ increases, V stays constant while p_e increases, until finally the system stabilizes at $p = p_e(\rho^*) - V = 0$, see Fig. 3. In this unstable phase, the system contracts until it stabilizes in the new ground state.

This instability leads to a "gap" in the predicted M–R relationship as seen in Fig. 2. The position of this gap is ϵ dependent; the smaller ϵ is, the more the gap is shifted toward small masses and large radii. We use the position of this gap to probe the existence of light QCD axions.

Note that the simplified discussion above is only valid for $R_{WD} \gg \lambda_\phi$. For $R_{WD} \sim \lambda_\phi$ we numerically solve the full coupled system in Eq. (12) and find that, for large values of the axion decay constant f, and small ϵ, the position of the gap is ϵ independent. This is understood as follows: on the stable branch, the gradient pressure, which is controlled by f, is relevant. If gravity is subdominant, this pressure fixes the central density of the star, $\rho(r = 0) > \rho^*$. The maximal radius is then achieved when the gravitational pressure equals the gradient pressure. For the metastable branch, the minimum radius is set by $R \sim \lim_{\epsilon \to 0} \lambda_\phi$.

Finally, in the limit $R_{WD} \ll \lambda_\phi$, the gradient energy is so large that the field cannot move away from its in-vacuum minimum and therefore has no influence on the structure of WDs.

C. Confrontation with observational data

There are large datasets available containing masses and radii of WDs (see, e.g., [14–20,32–38]). However, not all of these datasets can be used to probe the M–R relation. In some catalogs (see [32–36]), the M–R relation is used as an input to significantly reduce observational error. On the other hand, there are sets (e.g., [14–20,37,38]) that systematically test the M–R relation using observational data. While in [19] the determination of the mass and radius is completely independent of WD models, most other works depend on an atmospheric model to determine the radius. Nevertheless, we combine the datasets [14–20] and show them in Fig. 2.

The data of measured WD masses and radii are scattered broadly between radii of 5000 and 40000 km, which matches reasonably well with the free Fermi gas description. The notable deviation in mass found at large radii in Fig. 2 is due to finite temperature effects; μ_e in these dilute stars is typically smaller, increasing the relevance of T/μ_e corrections. Finite temperature effects lead to modifications of the EOS and to a slight modification of masses and radii, but still predict a continuous M–R curve. The same holds for other well-known corrections to the EOS, such as different compositions, electrostatic corrections, or nuclear reactions, see, e.g., Refs. [27,39]. While nuclear reactions change in the sourced phase, e.g., due to a different mass of the pions, this has negligible effect on the static structure of white dwarfs [40,41].

We perform a simplified statistical analysis to determine the compatibility of the observed WD radii with a gapped radius distribution hypothesis (marginalizing over mass and neglecting small theory systematics). We summarize here its main results, with the full details given in Appendix B. For the purpose of the analysis, we calculate the position of the radius gap as a function of ϵ and f, relying both on numerical results, as well as on numerically verified analytical estimates. In the region $f \ll 10^9$ GeV,

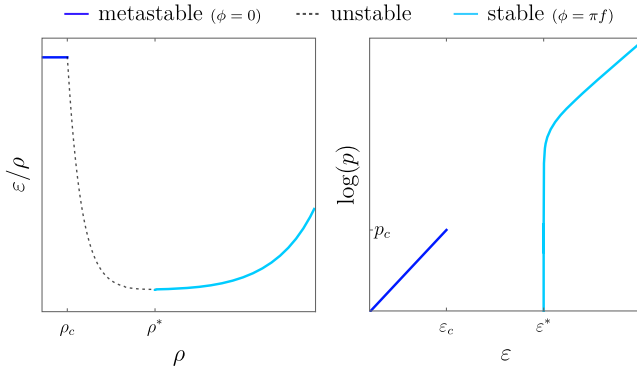FIG. 3. The energy per particle ε/ρ as a function of number density (left) and the EOS (right). At low densities $\rho < \rho_c$, the system is in its metastable $\phi = 0$ phase (dark blue). For $\rho_c < \rho < \rho^*$, the system is unstable, i.e., $p < 0$ (dashed line on left). At larger densities $\rho^* < \rho$, the system is in its $\phi = \pi f$ phase (light blue), with a new ground state at ε^*, where $p = 0$.

finite gradient effects are negligible with respect to the position of the gap, making it f independent. For the simplified model described in the main text, we are able to exclude at the 2σ level the following interval in ϵ,

$$2 \times 10^{-20} \lesssim \epsilon \lesssim 2 \times 10^{-7} \quad (95\% \text{ C.L.}), \quad (15)$$

see Fig. 1. On the other hand, for the $Z_{\mathcal{N}}$ model, our analysis (see Appendix C) leads to the exclusion of

$$33 \leq \mathcal{N} \leq 69 \quad (95\% \text{ C.L.}), \quad (16)$$

as shown in Fig. 12.

The upper limit is set by the smallest, most massive WDs and our analysis effectively excludes all points in the axion parameter space that cannot predict a WD with a radius smaller than around $\sim$4000 km on the metastable branch. The lower limit is sensitive to the largest, extremely low-mass WDs [20]. For even lower values of ϵ, the stable branch covers most of the range of observed radii. In this case, although all the observed WDs are sourcing the scalar field, the gap in radius is relegated to extremely large (and potentially unpopulated) WD radii. Note, however, that this region in parameter space is already ruled out by requiring that no sourcing occurs in our Sun [2].

Conversely, in the region $\epsilon \ll 10^{-20}$, or $\mathcal{N} \gg 71$, finite gradient effects are dominant with respect to the position of the gap, making it ϵ independent. Using solutions of the coupled system, Eq. (12), we are able to exclude at the 2σ level the following interval in f:

$$5.5 \times 10^9 < f/\text{GeV} < 1.1 \times 10^{16} \quad (95\% \text{ C.L.}), \quad (17)$$

see Fig. 1. The upper value represents the limit in which WDs are not large enough to source the scalar field, i.e., $\lambda_\phi \gtrsim R_{\text{WD}}$. In the region $f\epsilon^{-1/3} \sim M_{\text{P}}$, in which both gradient and finite ϵ effects are important, we verify numerically that the sourcing stops at lower values of f. Similar to the lower bound on ϵ, the lower bound on f is sensitive to the largest, extremely low-mass WDs. We stress again that we do not expect our results to strongly depend on finite temperature effects.

III. CONCLUSIONS

The mass-radius relationship of white dwarfs is well understood and has been observationally tested with increasing accuracy in recent years. We showed how light QCD axions change the structure of WDs, thus predicting the presence of a gap. We used existing data to place novel bounds on their parameter space. We stress that the bounds arising from the existence of a new ground state accessible in white dwarfs, and the corresponding gap in radii, are qualitatively very different than the strategy proposed in Ref. [2], which relies on the change of the properties of

nuclei, and the corresponding change in x-ray emission, when a (lighter) QCD axion is displaced to $\theta = \pi$ [40].

The QCD axion generically predicts a nonderivative coupling to nucleons. At finite baryon density this coupling can destabilize the axion from its in-vacuum minimum. If sourced, the nonzero axion expectation value reduces the mass of nucleons. For a large region of the parameter space, this leads to a new ground state of matter, which has less energy per particle than infinitely separated nucleons. If accessible in WDs, this drastically changes their M–R relation. Since the axion is sourced by the WD, this does not rely on the axion contributing to the dark matter relic abundance.

More precise tests of the WD M–R curve using the recent Gaia DR3 are expected in the near future and will further probe the parameter space of light QCD axions.

As a consequence of the new ground state of matter, we predict new small self-bound objects held together by the gradient pressure of the axion. These objects could give rise to novel signatures of exceptionally light QCD axions down to the QCD-axion line.

APPENDIX A: ANALYTIC ESTIMATES FOR THE RADIUS GAP

We define p_0 as the inward pointing pressure at the core of a white dwarf as a sum of a gravitational and a gradient contribution

$$p_0 \simeq \Delta p_{\text{grav}} + p_{\text{grad}}, \quad (A1)$$

with the gravitational pressure given by

$$\Delta p_{\mathrm{grav}} = \frac{R^2 m_N^2 \rho_0^2}{M_{\mathrm{P}}^2}, \qquad (\mathrm{A2})$$

where ρ_0 is the number density at the core ($r = 0$). The gradient pressure in the sourced phase (i.e., stars on the stable branch) is given by

$$p_{\mathrm{grad}} = \begin{cases} \frac{f^2}{R\lambda_\phi} = \frac{f\sqrt{\delta m_N \rho_R}}{R} & \lambda_\phi \ll R \\[2mm] \frac{f^2}{R^2} & \lambda_\phi \sim R \end{cases}, \qquad (\mathrm{A3})$$

where ρ_R is the number density at the edge ($r = R - \lambda_\phi \approx R$) of the WD. The first line in Eq. (A3) represents the thin wall limit $\lambda_\phi \ll R$, in which the gradient pressure is exerted at a small transition region at the edge of the star. In the last step, we use the definition of the in-medium wavelength of Eq. (13) assuming a negligible contribution from the scalar potential and neglecting $\mathcal{O}(1)$ factors. The second line in Eq. (A3) is the opposite regime $\lambda_\phi \sim R$, where the gradient pressure is delocalized and is spread throughout the star. This is the typical edge case configuration in which the star is barely large enough to source the axion. In the unsourced phase, i.e., stars on the metastable branch, $p_{\mathrm{grad}} = 0$. See Ref. [9] for more details on the derivation of Eqs. (A2) and (A3).

On the other hand, we define the outward pressure at the core balancing p_0, see Eq. (A1), as the contribution of the electron gas and the scalar potential, which can be written analytically in the nonrelativistic (NR) and ultrarelativistic (UR) limits as

$$p_0 \simeq -V(\phi) + p_e(\rho_0), \qquad (\mathrm{A4})$$

$$p_e(\rho_0) \simeq \begin{cases} \rho_0^{5/3}/m_e & (\mathrm{NR}\, \rho_0 \ll m_e^3) \\[2mm] \rho_0^{4/3} & (\mathrm{UR}\, \rho_0 \gg m_e^3) \end{cases}, \qquad (\mathrm{A5})$$

where in the sourced phase we have by definition $V(\phi) = p_e(\rho^*)$, while in the unsourced phase the scalar potential vanishes $V(\phi) = 0$. Note that in Eqs. (A2), (A3), and (A5), we work at leading order in $\delta m_N/m_N \ll 1$ and neglect $\mathcal{O}(1)$ numerical prefactors.

Let us start by estimating the minimal radius on the metastable branch, which we denote by $R_{\mathrm{min}}^{\mathrm{meta}}$, and the maximal radius on the stable branch, which we denote by $R_{\mathrm{max}}^{\mathrm{stable}}$, in the negligible gradient regime, where $\Delta p_{\mathrm{grav}} \gg p_{\mathrm{grad}}$. In this limit, $R_{\mathrm{max}}^{\mathrm{stable}}$ is the radius of the largest approximately constant energy density configurations. Therefore, we estimate it by setting $\rho_0 \approx c\rho^* \approx c\epsilon^{3/5}(m_e m_\pi^2 f_\pi^2)^{3/5}$, where $c \sim \mathcal{O}(1)$, and solving for R. The contribution to the pressure from $V(\phi) = p_e(\rho^*)$ is neglected since it is at most of the same order as $p_e(\rho_0)$ and would therefore have at most an $\mathcal{O}(1)$ effect on the final result. We find

$$R_{\mathrm{max}}^{\mathrm{stable}}(\epsilon) = \frac{M_{\mathrm{P}}}{m_N \Lambda_{\mathrm{QCD}}} \begin{cases} \left(\frac{\Lambda_{\mathrm{QCD}}}{m_e}\right)^{3/5} \epsilon^{-1/10} & (\mathrm{NR}) \\[2mm] \epsilon^{-1/4} & (\mathrm{UR}) \end{cases}, \qquad (\mathrm{A6})$$

where for brevity we denoted $m_\pi^2 f_\pi^2 \equiv \Lambda_{\mathrm{QCD}}^4$. We omit the weak dependence on c, which amounts to an $\mathcal{O}(1)$ prefactor. In the left panel of Fig. 4 we compare the analytic estimates to the numeric results. We find that the NR estimation is in excellent agreement with the numerical results for $\epsilon \lesssim 10^{-13}$ (red curve). For larger values of ϵ, the smaller minimal radii on the stable branch correspond to denser configurations, where relativistic corrections
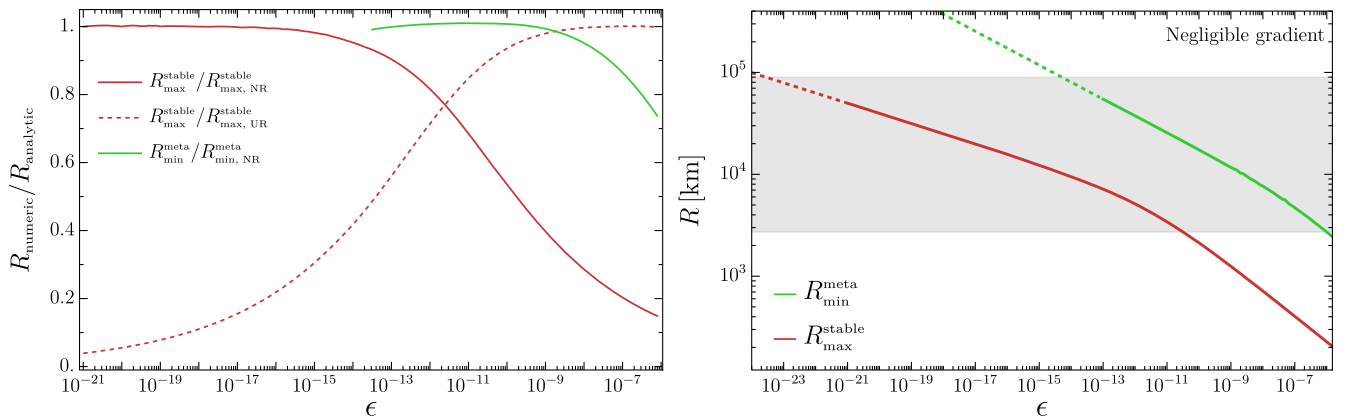

FIG. 4. Left: the ratio between the numerical results and the analytical estimates for the radii that correspond to the edges of the radius gap, as a function of ϵ. In (dashed) red we plot the ratio for $R_{\mathrm{max}}^{\mathrm{stable}}$ divided by the NR (UR) estimate given in Eq. (A6). In green we plot the ratio for $R_{\mathrm{min}}^{\mathrm{meta}}$, divided by the NR estimate give in Eq. (A7). In all cases we match the $\mathcal{O}(1)$ prefactors to the numerical results. Right: the radius gap defined by $R_{\mathrm{max}}^{\mathrm{stable}}$ (red) and $R_{\mathrm{min}}^{\mathrm{meta}}$ (green) as a function of ϵ. Solid curves indicate regions where numerical results are used, while the dashed curve indicates where extrapolation (using the verified analytic estimates) is used. The gray region corresponds to the observed radii range of WDs.
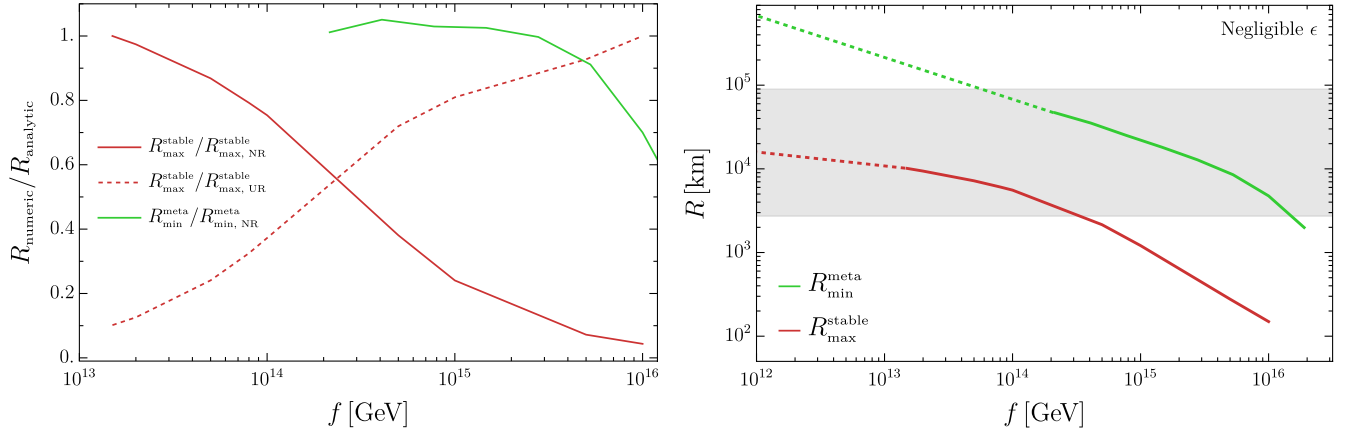
FIG. 5. Left: the ratio between the numerical results and the analytical estimates for the radii that correspond to the edges of the radius gap, as a function of f. In solid and dashed red, we plot the ratio for $R_\mathrm{max}^\mathrm{stable}$ divided by the NR and UR estimates given in Eqs. (A8) and (A9), respectively. In green, we plot the ratio for $R_\mathrm{min}^\mathrm{meta}$, divided by the NR estimate give in Eq. (A10). In all cases, we match the $\mathcal{O}(1)$ prefactors to the numerical results. Right: the radius gap defined by $R_\mathrm{max}^\mathrm{stable}$ (red) and $R_\mathrm{min}^\mathrm{meta}$ (green) as a function of f. Solid curves indicate regions where numerical results are used, while the dashed curve indicates where extrapolations (using the verified analytic estimates) are used. The gray region corresponds to the observed radii range of WDs.

become important. Thus, for $\epsilon \gtrsim 10^{-11}$ the UR estimation agrees with the numerical results (red dashed curve).

The edge of the metastable branch $R_\mathrm{min}^\mathrm{meta}$ is found by taking $\rho_0 \approx \rho_c \approx \epsilon \Lambda_\mathrm{QCD}^4/(2\sigma_N)$ and solving for R in the NR approximation, resulting in

$$R_\mathrm{min}^\mathrm{meta}(\epsilon) = \frac{M_\mathrm{P}}{m_N \Lambda_\mathrm{QCD}} \left(\frac{\sigma_N \Lambda_\mathrm{QCD}^2}{m_e^3} \right)^{1/6} \epsilon^{-1/6} \quad (\mathrm{NR}). \quad (A7)$$

A similar UR approximation is straightforward to derive. However, it is only valid for $R \ll M_\mathrm{P}/(m_N m_e) \sim 5000$ km, which is outside our range of interest. In the left panel of Fig. 4, we compare the analytic numerical results of $R_\mathrm{min}^\mathrm{meta}(\epsilon)$ to the analytic estimate. We find good agreement in most of the calculated region, namely, for $\epsilon \lesssim 10^{-9}$. For larger values, relativistic corrections start becoming important and the UR approximation begins to degrade.

The radius gap in the negligible gradient regime is plotted in the right panel of Fig. 4 as a function of ϵ. For the purpose of the analysis of Appendix B, solid curves indicate the regions where we use our numerical results, while dashed lines indicate regions where extrapolation, based on the verified numerical estimate, is used. The gray region corresponds to the observed radii range of WDs.

In the region of parameter space where ϵ is negligibly small (to be determined below), the position of the radius gap is determined by finite gradient effects. On one side, the edge of the metastable branch indicates when a region of size λ_ϕ with above-critical density is formed, which leads to an instability. On the other side, the largest configurations on the stable branch are those in which the gravitational pressure begins to dominate over the gradient pressure exerted at the edge of the star [9].

First, we find $R_\mathrm{max}^\mathrm{stable}$ for lower values of f where the thin-wall approximation holds, by taking $\rho_0 = \rho_R \equiv \rho_\mathrm{eq} > \rho^*$, where ρ_eq is found by solving $\Delta p_\mathrm{grav}(\rho_\mathrm{eq}) = \Delta p_\mathrm{grav}(\rho_\mathrm{eq})$ for ρ_eq. We than plug ρ_eq into Eq. (A1) and using the NR approximation of Eq. (A5) solve for R and find

$$R_\mathrm{max}^\mathrm{stable}(f) = \left(\frac{M_\mathrm{P}}{m_N} \right)^{7/6} \left(\frac{1}{\delta m_N^{1/12} f^{1/6} m_e^{3/4}} \right) \quad (\lambda_\phi \ll R),$$

$$(A8)$$

where we again neglect the contribution from $V(\phi)$ as an $\mathcal{O}(1)$ correction at most. We compare this estimate with the numerical results in Fig. 5 (red curve). We find it is consistent with the numerical results in the region $f \ll 10^{15}$ GeV. Above these values of f, the thin-wall approximation breaks down and $R_\mathrm{max}^\mathrm{stable}(f)$ can be estimated using the $\lambda_\phi \sim R$ expression for p_grav and the UR expression for the electron pressure, which gives us

$$R_\mathrm{max}^\mathrm{stable}(f) = \frac{M_\mathrm{P}^2}{m_N^2 f} \quad (\lambda_\phi \lesssim R). \quad (A9)$$

We find this estimate consistent with the numerical results in the region $f \gg 10^{15}$ GeV, see dashed curve in Fig. 5.

The edge of the metastable branch $R_\mathrm{min}^\mathrm{meta}$ is found by first finding the critical density for which the whole size of the star is of the order of the scalar in-medium wavelength, namely, by solving $\lambda_\phi(\rho) = f/\sqrt{\rho \delta m_N} = R$ for ρ and plugging the result in Eq. (A1) using the NR approximation for the electron gas. We find

$$R_{\min}^{\mathrm{meta}}(f) = \left(\frac{\delta m_N^{1/2} M_P^3}{f m_e^{3/2} m_N^3} \right)^{1/2}. \qquad (A10)$$

We find this estimate consistent with the numerical results, see green curve in Fig. 5. The deviations from the analytical estimate at large value of f is expected, since for smaller and denser stars relativistic corrections to the EOS become increasingly larger.

To conclude, we note that, for the whole $\{\epsilon, f\}$ plane, we define the maximal radius of the gap as

$$R_{\min}^{\mathrm{meta}}(\epsilon, f) = \mathrm{Min}\left[R_{\min}^{\mathrm{meta}}(\epsilon), R_{\min}^{\mathrm{meta}}(f) \right], \qquad (A11)$$

where the two radii coincide $R_{\min}^{\mathrm{meta}}(\epsilon) \sim R_{\min}^{\mathrm{meta}}(f)$ around the curve defined by

$$f \epsilon^{-1/3} \approx \frac{\sqrt{\delta m_N}}{\sqrt{m_e} m_N} \left(\frac{\Lambda_{\mathrm{QCD}}^4}{\sigma_N} \right)^{1/3} M_P \sim M_P, \qquad (A12)$$

using the NR estimations for both expressions. This defines (*a posteriori*) the ranges of validity for the negligible gradient and negligible ϵ approximations for the determination of $R_{\min}^{\mathrm{meta}}$, e.g., the negligible gradient is a valid approximation in the region of parameter space where $f \epsilon^{-1/3} \ll M_P$. Around $f \epsilon^{-1/3} \sim M_P$, we computed a numerical solution using the appropriate $\{\epsilon, f\}$ values in order to obtain $R_{\min}^{\mathrm{meta}}(\epsilon, f)$. In a similar fashion, we define for the whole $\{\epsilon, f\}$ plane the minimal radius of the gap as

$$R_{\max}^{\mathrm{stable}}(\epsilon, f) = \mathrm{Max}\left[R_{\max}^{\mathrm{stable}}(\epsilon), R_{\max}^{\mathrm{stable}}(f) \right], \qquad (A13)$$

where the two radii coincide $R_{\max}^{\mathrm{stable}}(\epsilon) \sim R_{\max}^{\mathrm{stable}}(f)$ around the curve defined by

$$f \epsilon^{-3/5} \approx \frac{\Lambda_{\mathrm{QCD}}^{12/5} M_P}{\sqrt{\delta m_N} m_e^{9/10} m_N} \sim 20 M_P, \qquad (A14)$$

using the NR estimations for both expressions. This defines (*a posteriori*) the ranges of validity for the negligible gradient and negligible ϵ approximations for the determination of $R_{\max}^{\mathrm{stable}}$.

APPENDIX B: STATISTICAL ANALYSIS AND BOUNDS

The goal is to quantitatively determine how compatible are the observed WD radii with a gapped distribution. Our working assumption is that the variance in the observed mass can be explained by varying other important properties of WDs, such as temperature and composition, which for simplicity we kept fixed. Therefore, our focus is strictly on the radius distribution, and in order to determine the bounds on ϵ and f, we perform a 1D goodness-of-fit test on the radius axis. Given the central values from a combined dataset of $N = 295$ observed WD radii $\{r_i\}$ and their corresponding uncertainties $\{\sigma_i\}$ [14–20], we calculate the sum of squares, which we denote by χ, for each point in the $\{\epsilon, f\}$ plane,

$$\chi(\epsilon, f) = \sum_{i=1}^{N} \frac{D^2\left[(r_i), R_{\max}^{\mathrm{stable}}(\epsilon, f), R_{\min}^{\mathrm{meta}}(\epsilon, f) \right]}{\sigma_i^2}, \qquad (B1)$$

with the distance function

$$D\left[(r_i), R_{\max}^{\mathrm{stable}}(\epsilon, f), R_{\min}^{\mathrm{meta}}(\epsilon, f) \right] = \begin{cases} \min\left[r_i - R_{\max}^{\mathrm{stable}}(\epsilon, f), R_{\min}^{\mathrm{meta}}(\epsilon, f) - r_i \right], & r_i \in \left[R_{\max}^{\mathrm{stable}}(\epsilon, f), R_{\min}^{\mathrm{meta}}(\epsilon, f) \right] \\ 0, & \mathrm{otherwise} \end{cases}. \qquad (B2)$$

We use the numerically calculated values for $\{ R_{\max}^{\mathrm{stable}}(\epsilon, f), R_{\min}^{\mathrm{meta}}(\epsilon, f) \}$ where available and otherwise use the verified analytical estimates as extrapolation; see right panels of Figs. 4 and 5.

In Figs. 6 and 7, we plot the results of our statistical analysis in the negligible gradient and negligible ϵ limits, respectively. In the left panels, we plot χ normalized to the effective number of degrees of freedom $N - 1$.

As a rough estimate, the range in which $\chi > 1$ is considered incompatible with the gapped radii distribution hypothesis. A more refined statement can be made by calculating the corresponding p values for each value of ϵ of f, shown in the right panels of Figs. 6 and 7, respectively. We are able to exclude at the 2σ level the following interval in ϵ:

$$2 \times 10^{-20} < \epsilon < 2 \times 10^{-7} \quad (95\% \ \mathrm{C.L.}). \qquad (B3)$$

We are able to exclude at the 2σ level the following interval in f:

$$5.5 \times 10^9 < f/\mathrm{GeV} < 1.1 \times 10^{16} \quad (95\% \ \mathrm{C.L.}). \qquad (B4)$$

APPENDIX C: $Z_{\mathcal{N}}$ AXION

The potential of lighter than expected QCD axions due to a $Z_{\mathcal{N}}$ discrete symmetry reads, in the large $\mathcal{N}$ limit [4],

$$V_{\mathcal{N}}(\theta) = -m_\pi^2 f_\pi^2 \sqrt{\frac{1-z}{1+z}} \frac{1}{\pi \mathcal{N}} z^{\mathcal{N}} [\cos(\mathcal{N}\theta) - 1], \qquad (C1)$$
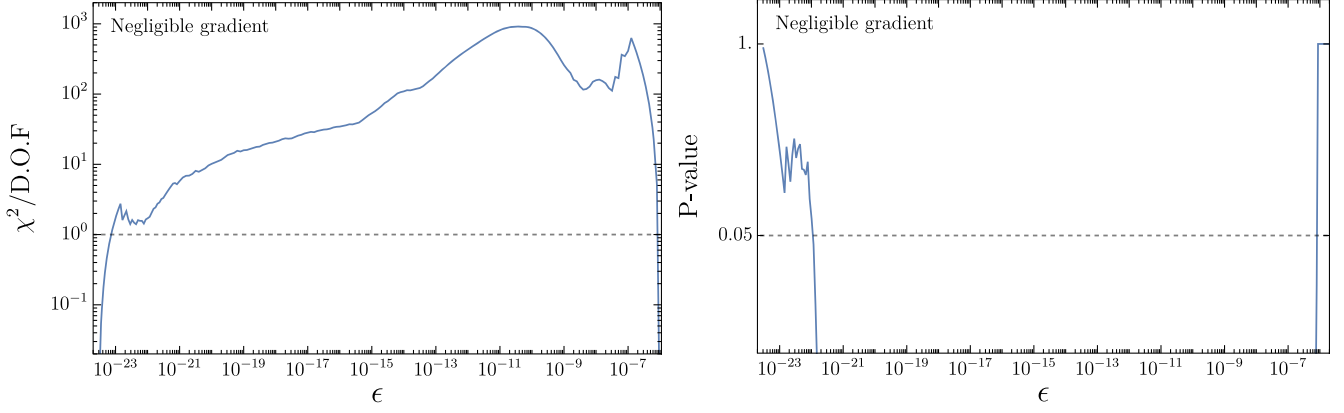
FIG. 6.   Left: $\chi(\epsilon)$, as defined in Eq. (B1) in the negligible gradient limit, normalized to the effective number of degrees of freedom $N - 1 = 294$, as a function of ϵ. Right: the p value as a function of ϵ. For reference, we plot the 2σ threshold, equivalent to $p = 0.05$, as a gray dashed line.
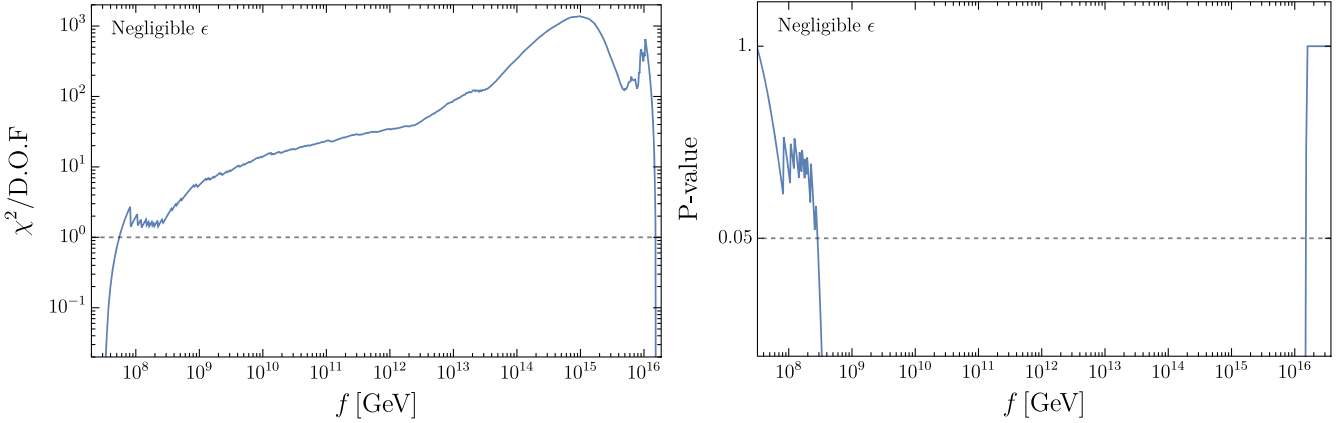
FIG. 7.   Left: $\chi(f)$, as defined in Eq. (B1) in the negligible ϵ limit, normalized to the effective number of degrees of freedom $N - 1 = 294$, as a function of f. Right: the p value as a function of f. For reference, we plot the 2σ threshold, equivalent to $p = 0.05$, as a gray dashed line.

where $\mathcal{N} \gg 1$ is odd and $z = m_u/m_d$. The corresponding axion mass reads

$$m_a^2 = \frac{\mathcal{N}^{3/2} z^{\mathcal{N}} \sqrt{1 - z^2}}{\sqrt{\pi}(1 + z)} \frac{m_\pi^2 f_\pi^2}{f^2}. \tag{C2}$$

We can map the $Z_{\mathcal{N}}$ axion to the potential in Eq. (2) by requiring equal axion masses. We find the relation

$$\epsilon = \frac{1}{\sqrt{\pi}} \mathcal{N}^{3/2} z^{\mathcal{N}-1}(1 + z)\sqrt{1 - z^2}. \tag{C3}$$

While this relation fixes the axion mass to be the same in both models, the value of the potential at $\theta = \pi$ is different. We find

$$V_{\mathcal{N}}(\pi) \simeq \frac{1}{\mathcal{N}^2} V(\pi), \tag{C4}$$

where $V(\theta)$ is the potential from Eq. (2). Clearly, there is a large suppression for $\mathcal{N} \sim \mathcal{O}(10)$, which is the scenario we are interested in.

At finite density $\rho = k_F^3/3\pi^2$, the potential for the $Z_{\mathcal{N}}$ axion is given by [4]

$$V_{\mathcal{N}}(\theta, \rho) = V_{\mathcal{N}}(\theta) + 2\sigma_{\pi N}\rho\sqrt{1 - \beta\sin^2\left(\frac{\theta}{2}\right)}, \tag{C5}$$

where $\beta = 4z/(1 + z)^2$. The critical density, at which the minimum at the origin is destabilized, i.e., $\partial_\theta^2 V_{\mathcal{N}}(0, \rho_c) = 0$ is

$$\rho_c = \frac{m_\pi^2 f_\pi^2}{2\sqrt{\pi}\sigma_{\pi N}} \mathcal{N}^{3/2} z^{\mathcal{N}-1}(1 + z)\sqrt{1 - z^2}, \tag{C6}$$

which matches the critical density for the potential in Eq. (2), $\rho_c = \epsilon m_\pi^2 f_\pi^2/2\sigma_{\pi N}$, with ϵ given by Eq. (C3).
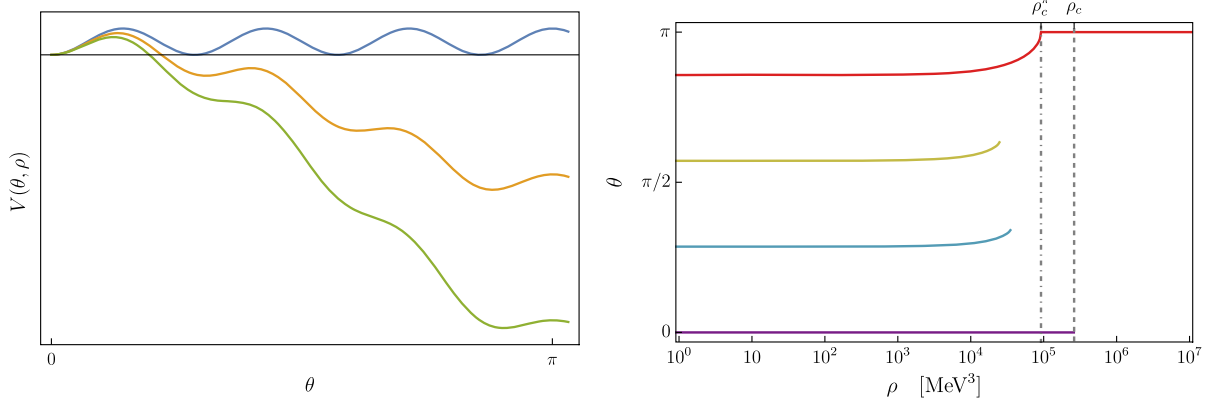
FIG. 8. Left: axion potential, Eq. (C5), for $\mathcal{N} = 7$, at zero density (blue), at finite density such that intermediate minima (at $\theta = 2\pi/7, \theta = 4\pi/7, \theta = 6\pi/7$) are present (orange), and at a subcritical finite density such that the intermediate minima are destabilized (green), see Eq. (C6). Right: $\theta(\rho)$ for $\mathcal{N} = 7$. Rainbow color coding marks the solutions to the $(7+1)/2 = 4$ minima from the one closest to π (red) to the one at zero (violet). The dot-dashed and dashed gray lines correspond to ρ_c^π and ρ_c, respectively.

At densities below the critical density, $V_{\mathcal{N}}(\theta, \rho)$ has $(\mathcal{N} + 1)/2$ minima in the interval $\theta \in [0, \pi]$, which we label by $k = 1, \ldots, (\mathcal{N} + 1)/2$.

At nonzero densities, minima with $k > 1$ have lower energy than the minimum at $\theta = 0$ (or $k = 1$), but get destabilized at lower densities than the minimum at $\theta = 0$. In particular, we would like to point out that $\theta = \pi$ is initially not the lowest energy configuration since it remains a maximum for these intermediate densities, hence it is not preferred over, e.g., $\theta = (\mathcal{N} - 1)\pi/\mathcal{N}$. We solve $\partial_\theta^2 V_{\mathcal{N}}(\pi, \rho_c^\pi) = 0$ and find that the density at which $\theta = \pi$ becomes the lowest energy configuration is

$$\rho_c^\pi = \frac{1 - z}{1 + z} \rho_c. \tag{C7}$$

At densities $\rho_c^\pi \le \rho \le \rho_c$, two minima exist, at $\theta = 0$ and $\theta = \pi$, while at densities $\rho > \rho_c$ the only remaining minimum is at $\theta = \pi$.

We show an $\mathcal{N} = 7$ potential for zero and subcritical densities in the left panel of Fig. 8. In the right panel, we show solutions $\theta(\rho)$ that sit in the $(\mathcal{N} + 1)/2$ minima between $\theta = 0$ and $\theta = \pi$ for $\mathcal{N} = 7$.

In the negligible gradient limit, we can derive the EOS as described in the main text, i.e., by solving Eq. (14). At subcritical densities we find $(\mathcal{N} + 1)/2$ independent branches of the EOS, one for each metastable minimum. The field value of θ increases with k and so does the reduction of the mass. The lowest energy configuration is therefore the branch that starts at $\theta = (\mathcal{N} - 1)\pi/\mathcal{N}$ at low densities.

Solving the system for all branches of the EOS, we generally find a qualitatively distinct behavior at small and large values of $\mathcal{N}$.

1. Small $\mathcal{N}$

At small $\mathcal{N}$, i.e., $\mathcal{N} \le 31$, the electron Fermi pressure dominates over the negative contribution from the potential, such that the total pressure stays positive. This is because electrons become relativistic at the relevant densities, since the lower the value of $\mathcal{N}$, the larger the critical density, see Eq. (C6).

Therefore, we do not find a gap in the EOS, which is qualitatively different from what we found for the potential in Eq. (2). We show the EOS, i.e., $p(\varepsilon)$, in the left panel of Fig. 9 for $\mathcal{N} = 31$. Note that the EOS for the branch that sits closest to π (red curve) does not experience a thermodynamic instability for any density, given that the pressure stays a monotonically increasing function of the energy density. Nevertheless, the onset of the nonzero potential once the field starts to be displaced reduces the pressure significantly, leading to a much softer EOS at large densities than the EOS for $\theta = 0$.

In the zero gradient limit, the M–R curve is readily found by solving the regular TOV equations (7) with the prescribed EOS. As expected from the EOS, we find continuous M–R curves. For very low values of $\mathcal{N}$, sourcing happens only for the densest WDs. We show the family of M–R branches in the right panel of Fig. 9 for $\mathcal{N} = 31$.

Even though the $(\mathcal{N} - 1)\pi/\mathcal{N}$ [i.e., $k = (\mathcal{N} + 1)/2$] branch encounters an instability in the M–R curve at intermediate radii (where $\partial M_{\mathrm{WD}}/\partial \rho_0 < 0$), the $\theta = 0$ branch covers these radii.

Since we are agnostic about the formation mechanism of the star, and thus of the branch it ends up after formation, a χ^2 in radii is not enough to exclude this prediction. In principle, an exclusion might be possible for the highest $\mathcal{N}$ in this regime, i.e., $\mathcal{N} = 31$. This requires a more sophisticated statistical analysis than done for the gapped curve and is beyond the scope of this work.
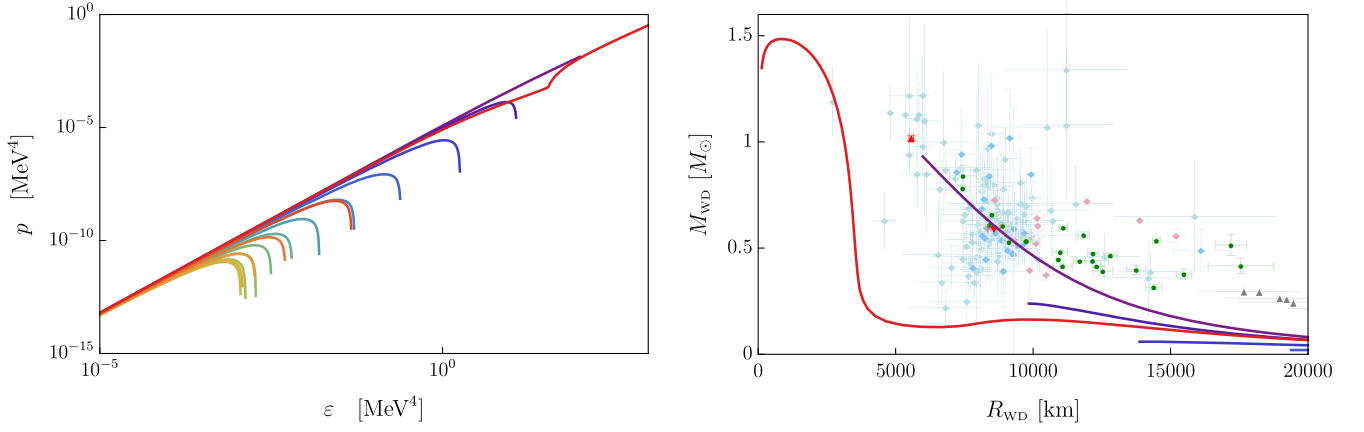
FIG. 9. Left: pressure as function of the energy density for $\mathcal{N} = 31$. Rainbow color coding marks the solutions to the $(31 + 1)/2 = 17$ minima from the one closes to π (most red) to the one at zero (most violet). The red curve never experiences negative pressure. While the pressure decreases due to the displacement of θ from $30\pi/31$, the Fermi pressure, due to electrons becoming relativistic, keeps the total pressure positive. Right: M–R curves for $\mathcal{N} = 31$ in the same color coding.

2. Large $\mathcal{N}$

At large $\mathcal{N}$, i.e., $\mathcal{N} \geq 33$, we find that the negative contribution of the potential dominates over the electron Fermi pressure. This implies a thermodynamic instability and a gap in the EOS, associated with a new ground state with density $\rho^* > \rho_c^\pi$. Contrary to the case of Eq. (2) (see Fig. 3), this gap can be covered by the $\theta = 0$ branch. This is because the $\theta = (\mathcal{N} - 1)\pi/\mathcal{N}$ minimum disappears (and the one at $\theta = \pi$ appears) before the minimum at $\theta = 0$ is destabilized, as follows from Eq. (C7). In Fig. 10, for $\mathcal{N} = 33$, it is shown that the region in which the instability occurs is covered for all densities by the metastable ($\theta = 0$) branch. For such $\mathcal{N}$, the new ground state density ρ^* lies below the critical density, as can be seen in the left panel of Fig. 10. For $\mathcal{N} \geq 39$, we find instead $\rho^* > \rho_c$, a scenario that parallels that discussed in the main text.

Analytic estimates for the density of the new ground state can be found by solving

$$p_e(\rho^*) - V_\mathcal{N}(\pi) = 0, \tag{C8}$$

in the nonrelativistic and ultrarelativistic limit. To leading order and neglecting $\mathcal{O}(1)$ numbers, these are given by

$$\rho_{\text{NR}}^* \simeq \left(\frac{z^\mathcal{N}}{\sqrt{\mathcal{N}}} \right)^{3/5} (m_e m_\pi^2 f_\pi^2)^{3/5}, \qquad k_F \ll m_e, \tag{C9}$$

$$\rho_{\text{UR}}^* \simeq \left(\frac{z^\mathcal{N}}{\sqrt{\mathcal{N}}} \right)^{3/4} (m_\pi^2 f_\pi^2)^{3/4}, \qquad k_F \gg m_e. \tag{C10}$$

As we have seen from the EOS, for larger values of $\mathcal{N}$ we find negative pressure phases in the $(\mathcal{N} - 1)\pi/\mathcal{N}$
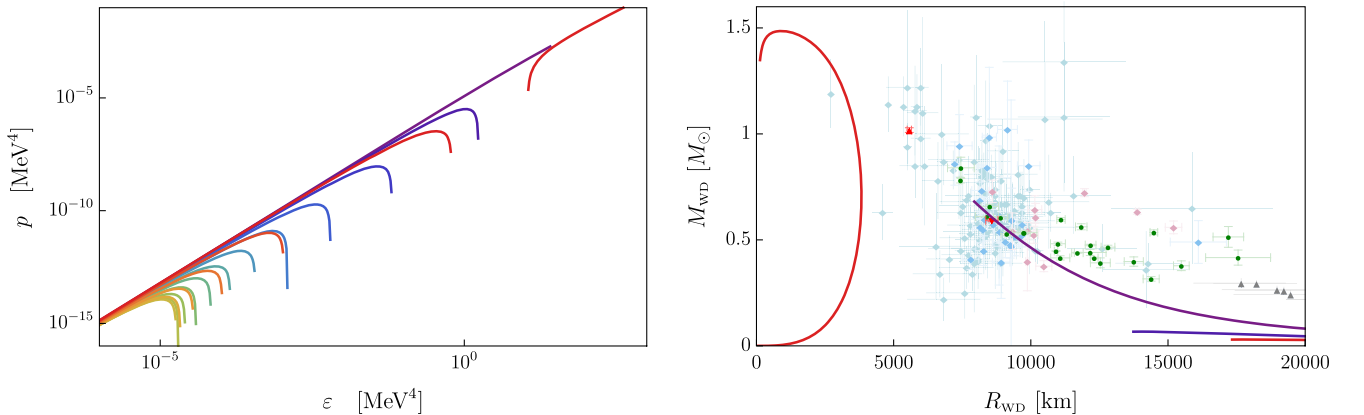

FIG. 10. Left: pressure as function of the energy density for $\mathcal{N} = 33$. The rainbow color coding marks the different branches of the EOS for the $(33 + 1)/2 = 17$ minima of θ with the ones closer to π being more red. Importantly, here the branch closest to π experiences an instability. Right: $M - R$ curves for $\mathcal{N} = 33$ in blue (SBO) and orange (metastable) and for the corresponding ϵ [Eq. (C3)] in green (SBO) and red (metastable).
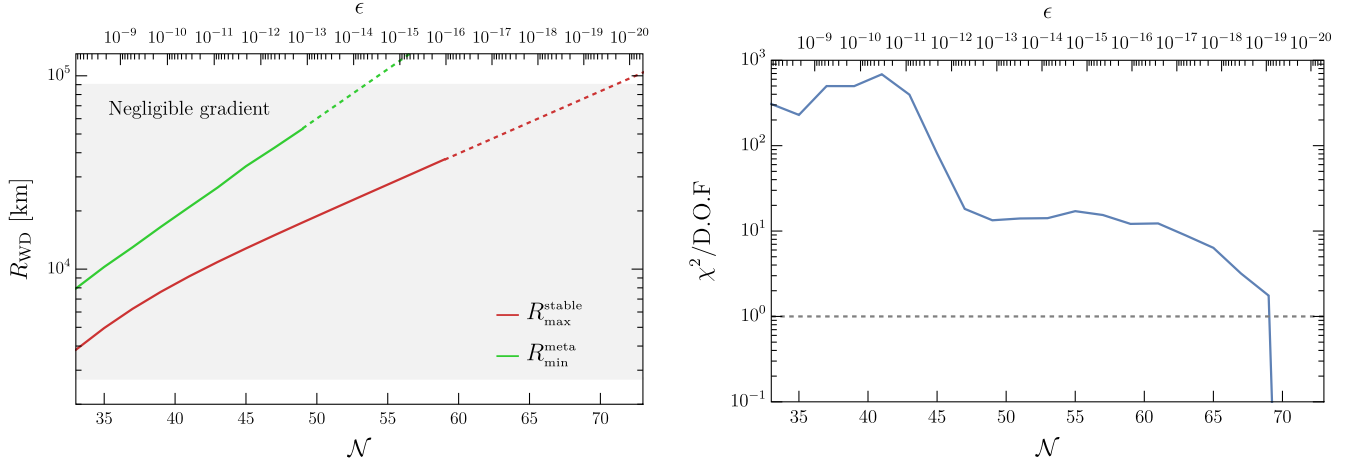
FIG. 11. Left: radius gap as a function of $\mathcal{N}$. Gray shaded area marks radii populated by data. Right: χ^2 values over data points in the gap as a function of $\mathcal{N}$.

branch. We therefore expect constant density self-bound objects (SBOs) and a gap in radii. In the left panel of Fig. 10 we show the EOS for $\mathcal{N} = 33$, which is the lowest $\mathcal{N}$ for which we find a new ground state (NGS). In the right panel of Fig. 10 we show the corresponding $M - R$ curves. As can be seen, the NGS leads to SBO solutions, i.e., the red curve that connects to $M_{\mathrm{WD}} = 0$ and $R_{\mathrm{WD}} = 0$. This branch is disconnected by a gap in radii from the metastable branches at larger radii.

In the left panel of Fig. 11 we show the gap in radii as a function of $\mathcal{N}$ for $\mathcal{N} \geq 33$. In green, we show the minimal radius of the metastable branch $R_{\mathrm{min}}^{\mathrm{meta}}$, where for very large radii we used the analytic estimate

$$R_{\mathrm{min}}^{\mathrm{meta}} \simeq 10^4 \left(\frac{2 m_N \rho_c}{10^6 \ \mathrm{g \, cm}^{-3}} \right)^{-1/6} \ \mathrm{km}, \qquad \text{(C11)}$$

see, e.g., [39]. In red, we show the maximal radius of the stable branch $R_{\mathrm{max}}^{\mathrm{stable}}$ for which we use our numerical results and a similar analytic estimate

$$R_{\mathrm{max}}^{\mathrm{stable}} \simeq \frac{M_{\mathrm{P}}}{m_N \sqrt{m_e}} \left(\frac{1}{\rho_{\mathrm{NR}}^*} \right)^{1/6}. \qquad \text{(C12)}$$

In the right panel of Fig. 11 we show the results of the χ^2 analysis, described in Appendix B. As can be seen,
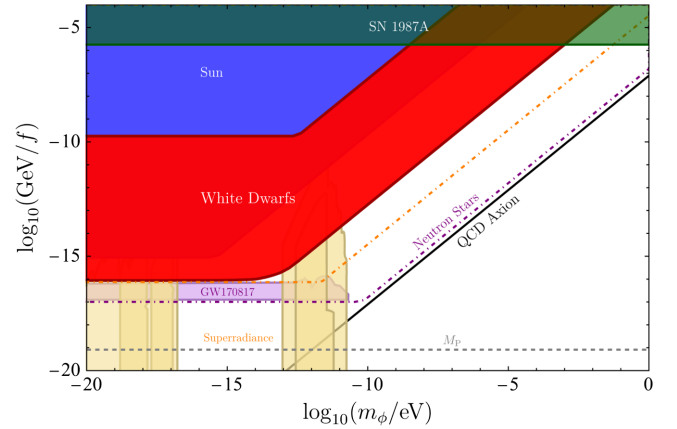

FIG. 12. Constraints and future projections on the axion parameter space for the $Z_{\mathcal{N}}$ model. Same as in Fig. 1.

at the 95% confidence level, we are able to exclude $33 \leq \mathcal{N} \leq 69$.

Last, we expect gradient effects to be of similar importance as in the detailed study above for only one minimum. Thus, we expect also for the $Z_{\mathcal{N}}$ axion that the bound shuts down similarly around $f \sim 10^{16}$ GeV. With an analogous statistical analysis as done above, we come to a slightly modified bound, as is shown in Fig. 12.

[1] In Eqs. (2) and (3), we show approximated expressions using $\cos(\phi/f)$. In practice, we used the more accurate expressions [42]

$$V = -\epsilon m_\pi^2 f_\pi^2 \left(\sqrt{1 - \frac{4m_u m_d}{(m_u + m_d)^2} \sin^2\left(\frac{\phi}{2f}\right)} - 1 \right),$$

and

$$\mathcal{L} = -\sigma_N \bar{N}N \left(\sqrt{1 - \frac{4m_u m_d}{(m_u + m_d)^2} \sin^2\left(\frac{\phi}{2f}\right)} - 1 \right).$$

[2] A. Hook and J. Huang, Probing axions with neutron star inspirals and other stellar processes, J. High Energy Phys. 06 (2018) 036.

[3] A. Hook, Solving the hierarchy problem discretely, Phys. Rev. Lett. **120,** 261802 (2018).

[4] L. Di Luzio, B. Gavela, P. Quilez, and A. Ringwald, An even lighter QCD axion, J. High Energy Phys. 05 (2021) 184.

[5] L. Di Luzio, B. Gavela, P. Quilez, and A. Ringwald, Dark matter from an even lighter QCD axion: Trapped misalignment, J. Cosmol. Astropart. Phys. 10 (2021) 001.

[6] A. Banerjee, J. Eby, and G. Perez, From axion quality and naturalness problems to a high-quality $\mathbb{Z}_{4\mathcal{N}}$ QCD relaxion, Phys. Rev. D **107,** 115011 (2023).

[7] R. Balkin, J. Serra, K. Springmann, and A. Weiler, The QCD axion at finite density, J. High Energy Phys. 07 (2020) 221.

[8] R. Balkin, J. Serra, K. Springmann, S. Stelzl, and A. Weiler, Density induced vacuum instability, SciPost Phys. **14,** 071 (2023).

[9] R. Balkin, J. Serra, K. Springmann, S. Stelzl, and A. Weiler, Heavy neutron stars from light scalars, arXiv:2307 .14418.

[10] C. Gao and A. Stebbins, Structure of stellar remnants with coupling to a light scalar, J. Cosmol. Astropart. Phys. 07 (2021) 025.

[11] J. Zhang, Z. Lyu, J. Huang, M. C. Johnson, L. Sagunski, M. Sakellariadou, and H. Yang, First constraints on nuclear coupling of axionlike particles from the binary neutron star gravitational wave event GW170817, Phys. Rev. Lett. **127,** 161101 (2021).

[12] G. Lucente, L. Mastrototaro, P. Carenza, L. Di Luzio, M. Giannotti, and A. Mirizzi, Axion signatures from supernova explosions through the nucleon electric-dipole portal, Phys. Rev. D **105,** 123020 (2022).

[13] A. Arvanitaki, M. Baryakhtar, and X. Huang, Discovering the QCD axion with black holes and gravitational waves, Phys. Rev. D **91,** 084011 (2015).

[14] A. Bédard, P. Bergeron, and G. Fontaine, Measurements of physical parameters of white dwarfs: A test of the mass-radius relation, Astrophys. J. **848,** 11 (2017).

[15] P.-E. Tremblay, N. Gentile-Fusillo, R. Raddi, S. Jordan, C. Besson, B. T. Gänsicke, S. G. Parsons, D. Koester, T. Marsh, R. Bohlin, J. Kalirai, and S. Deustua, The Gaia DR1 mass-radius relation for white dwarfs, Mon. Not. R. Astron. Soc. **465,** 2849 (2016).

[16] S. R. G. Joyce, M. A. Barstow, S. L. Casewell, M. R. Burleigh, J. B. Holberg, and H. E. Bond, Testing the white dwarf mass-radius relation and comparing optical and far-UV spectroscopic results with Gaia DR2, HST, and FUSE, Mon. Not. R. Astron. Soc. **479,** 1612 (2018).

[17] H. E. Bond, R. L. Gilliland, G. H. Schaefer, P. Demarque, T. M. Girard, J. B. Holberg, D. Gudehus, B. D. Mason, V. Kozhurina-Platais, M. R. Burleigh, M. A. Barstow, and E. P. Nelan, Hubble space telescope astrometry of the Procyon system, Astrophys. J. **813,** 106 (2015).

[18] H. E. Bond, G. H. Schaefer, R. L. Gilliland, J. B. Holberg, B. D. Mason, I. W. Lindenblad, M. Seitz-McLeese, W. D. Arnett, P. Demarque, F. Spada, P. A. Young, M. A. Barstow, M. R. Burleigh, and D. Gudehus, The Sirius system and its astrophysical puzzles: Hubble space telescope and ground-based astrometry, Astrophys. J. **840,** 70 (2017).

[19] S. G. Parsons *et al.*, Testing the white dwarf mass-radius relationship with eclipsing binaries, Mon. Not. R. Astron. Soc. **470,** 4473 (2017).

[20] W. R. Brown, M. Kilic, A. Kosakowski, J. J. Andrews, C. O. Heinke, M. A. Agüeros, F. Camilo, A. Gianninas, J. J. Hermes, and S. J. Kenyon, The ELM survey. VIII. Ninety-eight double white dwarf binaries, Astrophys. J. **889,** 49 (2020).

[21] S. i. P. Nunes, J. D. V. Arbañil, and M. Malheiro, The structure and stability of massive hot white dwarfs, Astrophys. J. **921,** 138 (2021).

[22] S. M. de Carvalho, M. Rotondo, J. A. Rueda, and R. Ruffini, Relativistic Feynman-metropolis-teller treatment at finite temperatures, Phys. Rev. C **89,** 015801 (2014).

[23] G. Shaviv and A. Kovetz, The thermodynamics of white dwarf matter II., Astron. Astrophys. **16,** 72 (1972).

[24] A. Kovetz and G. Shaviv, The thermodynamics of white dwarf matter, Astron. Astrophys. **8,** 398 (1970).

[25] D. Q. J. Lamb, Evolution of pure 12C white dwarfs, Technical Report, U.S., 1974.

[26] D. Q. Lamb and H. M. van Horn, Evolution of crystallizing pure ^{12}C white dwarfs, Astrophys. J. **200,** 306 (1975).

[27] D. Koester and G. Chanmugam, Review: Physics of white dwarf stars, Rep. Prog. Phys. **53,** 837 (1990).

[28] J. R. Oppenheimer and G. M. Volkoff, On massive neutron cores, Phys. Rev. **55,** 374 (1939).

[29] R. C. Tolman, Static solutions of Einstein's field equations for spheres of fluid, Phys. Rev. **55,** 364 (1939).

[30] The interesting case of a scalar coupled nonderivatively to electrons inducing a ϕ-dependent mass $m_e^*(\phi)$ is left for a separate publication [43].

[31] E. Witten, Cosmic separation of phases, Phys. Rev. D **30,** 272 (1984).

[32] N. P. G. Fusillo, P.-E. Tremblay, E. Cukanovaite, A. Vorontseva, R. Lallement, M. Hollands, B. T. Gänsicke, K. B. Burdge, J. McCleery, and S. Jordan, A catalogue of white dwarfs in Gaia EDR3, Mon. Not. R. Astron. Soc. **508,** 3877 (2021).

[33] J. Madej, M. Nalezyty, and L. G. Althaus, Mass distribution of DA white dwarfs in the first data release of the Sloan Digital Sky Survey, Astron. Astrophys. **419,** L5 (2004).

[34] M. Nalezyty and J. Madej, A catalogue of isolated massive white dwarfs, Astron. Astrophys. **420,** 507 (2004).

[35] D. Koester and S. O. Kepler, Carbon-rich (DQ) white dwarfs in the Sloan Digital Sky Survey, Astron. Astrophys. **628,** A102 (2019).

[36] F. M. Jiménez-Esteban, S. Torres, A. Rebassa-Mansergas, G. Skorobogatov, E. Solano, C. Cantero, and C. Rodrigo, A white dwarf catalogue from Gaia-DR2 and the Virtual Observatory, Mon. Not. R. Astron. Soc. **480,** 4505 (2018).

[37] P. Bergeron, P. Dufour, G. Fontaine, S. Coutu, S. Blouin, C. Genest-Beaulieu, A. Bédard, and B. Rolland, On the measurement of fundamental parameters of white dwarfs in the Gaia era, Astrophys. J. **876,** 67 (2019).

[38] C. Genest-Beaulieu and P. Bergeron, A comprehensive spectroscopic and photometric analysis of DA and DB white dwarfs from SDSS and Gaia, Astrophys. J. **871,** 169 (2019).

[39] S. L. Shapiro and S. A. Teukolsky, *Black Holes, White Dwarfs, and Neutron Stars: The Physics of Compact Objects* (Wiley, New York, 1983).

[40] L. Ubaldi, Effects of theta on the deuteron binding energy and the triple-alpha process, Phys. Rev. D **81,** 025011 (2010).

[41] In this work we take a conservative approach and stay agnostic of the process of formation of the new ground state phase, where the change of nuclear reactions could play a role.

[42] G. Grilli di Cortona, E. Hardy, J. Pardo Vega, and G. Villadoro, The QCD axion, precisely, J. High Energy Phys. 01 (2015) 034.

[43] R. Balkin, J. Serra, K. Springmann, S. Stelzl, and A. Weiler, White dwarfs as a probe of non-derivative scalar electron couplings (to be published).